

A Grid-Refinement-Based Approach for Modeling the Convective Boundary Layer in the Gray Zone: Algorithm Implementation and Testing

BOWEN ZHOU

Key Laboratory for Mesoscale Severe Weather, Ministry of Education, and School of Atmospheric Sciences, Nanjing University, Nanjing, China

MING XUE

Key Laboratory for Mesoscale Severe Weather, Ministry of Education, and School of Atmospheric Sciences, Nanjing University, Nanjing, China, and Center for Analysis and Prediction of Storms, and School of Meteorology, University of Oklahoma, Norman, Oklahoma

KEFENG ZHU

Key Laboratory for Mesoscale Severe Weather, Ministry of Education, and School of Atmospheric Sciences, Nanjing University, Nanjing, China

(Manuscript received 21 November 2017, in final form 24 January 2018)

ABSTRACT

A grid-refinement-based method is implemented in a community atmospheric model to improve the representation of convective boundary layer (CBL) turbulence on gray-zone [i.e., $\sim O(1)$ km] grids. At this resolution, CBL convection is partially resolved and partially subgrid scale (SGS), such that neither traditional mesoscale planetary boundary layer (PBL) schemes nor SGS closures for large-eddy simulations (LESs) are appropriate. The proposed method utilizes two-way interactive nesting to refine the horizontal resolution of the unstable surface layer of the daytime CBL. SGS turbulent mixing in the fine nest and coarse parent grids are parameterized by an LES turbulence closure and a PBL scheme, respectively. The method does not rely on predetermined empirical functions to introduce grid (scale) dependency and in theory works with any PBL scheme. Compared to the stand-alone gray-zone simulation, the proposed approach shows improvements in terms of higher-order statistics, the timing of the onset of resolved convection, and the convective structures. A deficiency of the method exists when the nest domain is limited to the surface layer; the convective structures become gradually contaminated by spurious convection on the parent gray-zone grid. A deeper nest domain alleviates the issue at increased computational costs.

1. Introduction

The model gray zone refers to the range of grid spacing that is comparable to the characteristic length scale of the flow (Wyngaard 2004; Arakawa et al. 2011). As the characteristic flow becomes partially resolved and partially subgrid scale (SGS) in the gray zone, ensemble-based schemes are inappropriate to parameterize the unresolved flow because of the lack of homogeneity within the grid cell. On the other hand, turbulence closures for large-eddy simulations (LESs) are inapplicable because the most energetic flow is too poorly resolved. As such, no conventional choices are

available to parameterize the SGS motions on the gray-zone grid. Therefore, the gray zone is also named *terra incognita* by Wyngaard (2004).

In the daytime convective boundary layer (CBL), the boundary layer depth z_i characterizes the length scale of organized convective circulations (Lenschow and Stankov 1986) and hence defines the CBL gray zone. For typical daytime conditions over land, z_i can grow to about 1–2 km (Kaimal and Finnigan 1994). To improve the representation of CBL turbulent mixing in the gray zone, an approach based on grid nesting was suggested in Zhou et al. (2017). In that study, they investigated the role of the unstable surface layer (bottom 10%–15% of the CBL; see Stull 1988, chapter 11) in the daytime CBL driven by surface heating. Based on solutions of a

Corresponding author: Bowen Zhou, zhoubowen@nju.edu.cn

DOI: 10.1175/JAS-D-17-0346.1

© 2018 American Meteorological Society. For information regarding reuse of this content and general copyright information, consult the [AMS Copyright Policy](https://www.ametsoc.org/PUBSReuseLicenses) (www.ametsoc.org/PUBSReuseLicenses).

simplified analytic model of the CBL and one-way nested simulations with refined surface-layer resolution, they demonstrated that surface-layer instabilities largely control the onset of buoyant convection and organized convective structures in the mixed layer. Their findings suggest that if surface-layer convection can be properly resolved, the overall simulation of the CBL in the gray zone is expected to improve qualitatively. Based on this, a vertically two-way nested configuration of finer horizontal resolution is implemented in a community atmospheric model to explicitly resolve convection in the surface layer to improve gray-zone simulations of the CBL.

Grid nesting has often been used to improve the representation of critical layers or zoom in to small-scale flow features of interest. It represents a computationally efficient and economical way of allocating grid cells where they are needed (Zhong and Chow 2012). In particular, grid nesting has been adopted to increase the resolution of the surface layer for LESs, where the size of turbulent eddies is strongly suppressed by the presence of the boundary (Sullivan et al. 1996; Huq et al. 2014). For example, Sullivan et al. (1996) applied a two-way nested grid in an LES to enhance the resolution of near-wall turbulence in a strongly sheared and weakly buoyant CBL. They observed improvements of turbulence statistics and spectra within the surface layer but no appreciable difference above, to which they suggested that small-scale features (relative to the LES grid) in the surface layer do not propagate far upward into the mixed layer.

This work is different from the previous studies that utilize grid refinement as a wall model for LES. On the LES grid, the most energetic eddies are well resolved. Higher resolution in the surface layer improves the representation of small-scale turbulence but hardly affects the overall boundary layer simulation as remarked by Sullivan et al. (1996). However, on the gray-zone grid, the dominant convective eddies are only partially resolved, let alone smaller-scale motions. Therefore, a resolved surface layer qualitatively changes the dynamics of the surface layer, which in turn influences the mixed layer above, because the large boundary layer convective eddies do span the entire depth of the CBL (Hunt et al. 1988).

2. Numerical methods

A two-way vertical nest algorithm is implemented in the Advanced Regional Prediction System (ARPS; Xue et al. 2000, 2001). ARPS is developed at the Center for Analysis and Prediction of Storms at the University of Oklahoma and is a nonhydrostatic finite-difference model suitable for simulations/predictions ranging from LES through regional numerical weather prediction.

More details about ARPS are documented in Xue et al. (2000, 2001). To our knowledge, most community atmospheric models do not have a two-way vertical nesting capability. The Regional Atmospheric Modeling System (RAMS; Pielke et al. 1992) is one of a few models with two-way interactive nesting that can be limited in the vertical extent (Walko et al. 1995), although the purpose of its grid nesting had not been for improving CBL turbulent mixing. ARPS allows for one-way nesting, where the parent and the nested simulations are performed sequentially. The nest domain can be shallower than the parent domain. The grid configuration of the nest domain is also independent from that of the parent domain. The Weather Research and Forecasting (WRF) Model allows for both one-way and two-way nesting (Skamarock et al. 2008). In the latter, the extent of the vertical domain and the vertical grid levels have to be identical in the parent and the nested grids. Recently, Lundquist et al. (2016) developed algorithms that allow the nest domain to have denser vertical levels, which alleviates numerical errors due to large aspect ratios on coarse grids and improves the accuracy on the nest domain.

A two-way vertical nesting capability implemented for the purpose of improving gray-zone turbulence parameterization is potentially useful for other modeling applications also. For example, for the nighttime stable boundary layer (SBL) flow over the Great Plains, the boundary layer depth usually ranges from 100 to 500 m (Stull 1988, chapter 12.1.2) and, in some extremely stable cases, is of order 1 m (Mahrt 2014). When simulating such an SBL, it is not necessary to have a nest domain that extends to the full depth of the model domain. A shallow vertically nested domain is a much more computationally efficient way of allocating grid points or, in other words, limited computational resources.

a. Grid setup

A 2D schematic of the grid setup is presented here in Fig. 1. The nested grid extends from vertical level 1 to n_z . The rest of the parent grid from vertical level $n_z + 1$ to N_z remains unchanged. Within the nested grid, the top n_{rz} levels are assigned to the relaxation zone to ensure a smooth transition between the coarse and fine grids. The horizontal grid spacings of the nested and parent grids are $\delta_{x,y}$ and $\Delta_{x,y}$, respectively, where $\Delta_{x,y}$ is an odd integer multiple of $\delta_{x,y}$. For the current work, the lateral boundaries of the two grids are the same, although this is not required. Horizontal nesting can be implemented together with vertical nesting. The vertical levels of the nested grid are identical to those of the parent grid. Vertical grid refinement in the nested grid is usually not necessary since in mesoscale models, Δ_z is often 50 m or

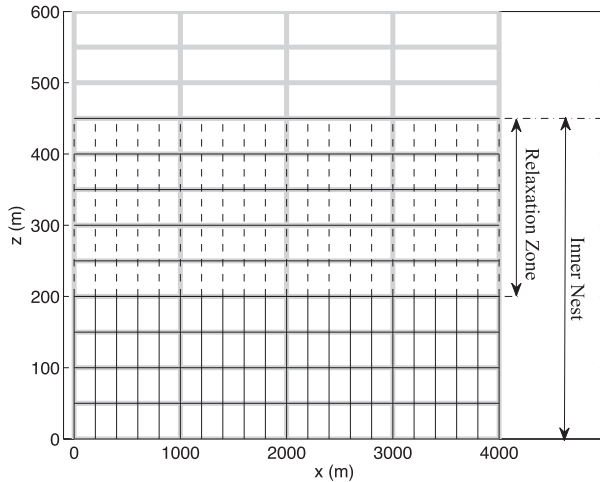


FIG. 1. A 2D schematic of the vertically nested gray-zone grid. Thick and thin lines represent the coarse and fine grids, respectively. The nested grid occupies the bottom 10 levels, the top 5 of which belong to the relaxation zone. The horizontal spacings are 1000 and 200 m for the parent and nest grid, respectively, with a refinement ratio of 5. The vertical spacing is 50 m. The parent grid above 600 m is not shown for brevity.

less with the employment of a vertically stretched grid. As such, Δ_z is already much finer than $\Delta_{x,y}$, and the latter is the primary limiting factor in resolving CBL convection (Ching et al. 2014; Zhou et al. 2014). However, refining vertical resolution can be important for nested

grids; for example, Brasseur and Wei (2010) and Daniels et al. (2016) show that an optimized choice of the surface-grid aspect ratios can yield improved agreement with surface similarity theories. If needed, further refinement of the grid in the vertical can be implemented following Daniels et al. (2016).

b. Solution algorithm

The step-by-step procedures of the nested grid algorithm are outlined in Fig. 2. Details are given below.

1) STEP 1

Prognostic variables on the nested grid are initialized with bilinear interpolation in the horizontal directions from the coarse parent grid. The initialization can be performed at any user-specified time. Here, the nested grid is initiated at time zero from a horizontally uniform base state to study its effects on the onset of convection. In this case, higher-order schemes yield the same results as linear interpolation and therefore are not tested in this work. Random potential temperature perturbations of ± 0.1 -K magnitude are applied at the lowest model level to initiate turbulent flows.

2) STEPS 2–3

The surface fluxes in the parent domain are computed with the surface drag formulation based on Monin–Obukhov similarity theory:

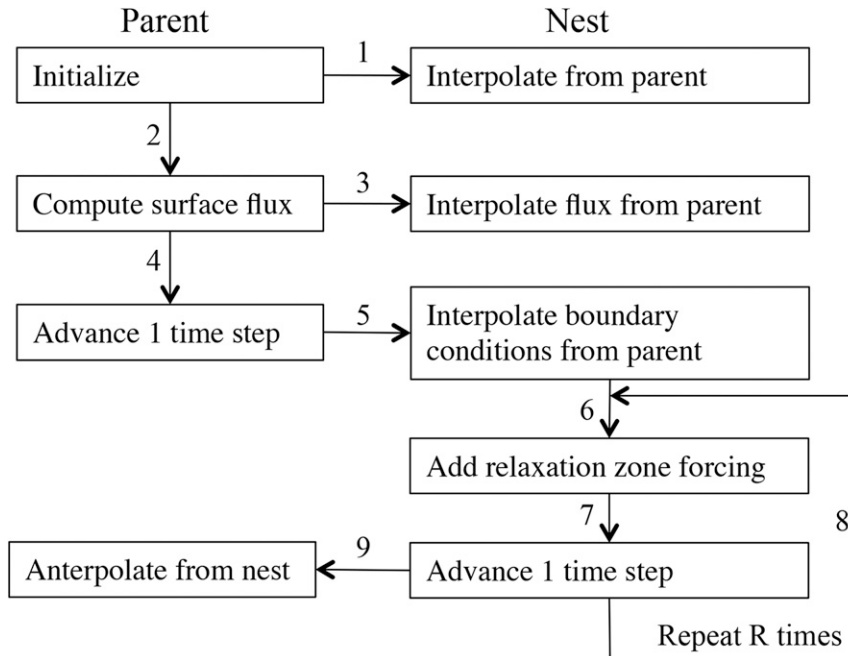


FIG. 2. Flowchart of the solution algorithm. The numbers indicate the sequence of the flowchart.

$$\overline{w'\phi'_s} = -C_\phi U_1(\phi_1 - \phi_s), \quad (1)$$

where ϕ is a generic variable, $\overline{w'\phi'}$ is the vertical turbulent flux of ϕ , C_ϕ is the drag coefficient for ϕ , U is the wind speed, and subscripts s and 1 represent the surface and the first grid point above the ground surface, respectively. In the nested grid, the surface fluxes are not computed locally but interpolated from the parent grid. The interpolation procedure [see Eq. (3) below] conserves domain-averaged fluxes. Doing so ensures the same amount of surface flux going into (or leaving) the shared bottom boundary of the parent and nest grids, although this is at the cost of a loss of resolvable surface heterogeneity on the fine nested grid.

When surface fluxes are computed locally on the nest domain, additional heterogeneity is introduced through locally varying surface fluxes. This is favorable for the development of finescale turbulence. However, biases in surface winds and temperature can also arise because of deficiencies of turbulence closures near the wall (Moeng et al. 2007; Mirocha et al. 2013). Ideally, as the flow transitions between the parent and nested grids, the partition of fluxes between the resolved and subgrid scale changes based on the grid resolution, while the total flux is conserved. However, since SGS turbulence closures are often deficient near the bottom boundary where the flow is poorly resolved (Chow et al. 2005), the total flux might change, leading to different turbulent mixing, hence creating biases in prognostic variables. To investigate the effects of locally formulated fluxes, a separate test is performed, and the results are discussed in section 4.

3) STEPS 4–5

ARPS uses a mode-splitting time integration scheme (Klemp and Wilhelmson 1978). The large time steps Δt use the leapfrog or a third-order Runge–Kutta method. First-order forward–backward explicit time stepping is used for the small steps $\Delta \tau$ to accommodate high-frequency acoustic waves. Terms responsible for the vertical acoustic propagation are treated implicitly. This work uses the leapfrog method for advancing large time steps in both the parent and nested grids. Adapting the code to a third-order Runge–Kutta scheme is straightforward.

Prognostic variables at the nest domain top are interpolated from the parent onto the nested grid as the top boundary conditions. In addition, interpolation is also applied to those in the relaxation zone for computing relaxation forcings in step 6. Interpolation is constrained by the conservation condition of Kurihara et al. (1979):

$$\langle \phi \rangle = \langle \Phi \rangle, \quad (2)$$

where ϕ and Φ are variables on the nest and parent grid, respectively, and $\langle \rangle$ refers to horizontal averaging. Conservation is enforced globally across the parent–nest grid interface. An interpolation formula that satisfies Eq. (2) is the second-order scheme of Clark and Farley (1984). Its one-dimensional (1D) form is presented for brevity:

$$\begin{aligned} \phi &= E_- \Phi_- + E_0 \Phi_0 + E_+ \Phi_+, \\ E_- &= \varepsilon(\varepsilon - 1)/2 + \alpha, \\ E_0 &= (1 - \varepsilon^2) - 2\alpha, \\ E_+ &= \varepsilon(\varepsilon + 1)/2 + \alpha, \quad \text{and} \\ \alpha &= \left[\left(\frac{\delta}{\Delta} \right)^2 - 1 \right] / 24, \end{aligned} \quad (3)$$

where the subscript 0 refers to the center grid point on the coarse grid and subscripts $-$ and $+$ refer to one coarse-grid interval above and below the center grid point. Here, E represents the weights on the three neighboring coarse-grid points; $\varepsilon = i/R_x$ is the normalized distance between the fine-grid and center coarse-grid points, where R_x is an odd integer nesting ratio, and i takes integer values from $-(R_x - 1)/2$ to $(R_x - 1)/2$. The variable α is a correction factor to the second-order interpolation. This particular choice of α in Eq. (3) satisfies the conservation (aka, reversibility) condition across the grid interface (Kurihara et al. 1979).

In addition to Eq. (2), it is further required that resolved vertical fluxes satisfy a similar conservation constraint:

$$\langle w'\phi' \rangle = \langle W'\Phi' \rangle. \quad (4)$$

More strictly, the conservation of vertical fluxes should be enforced on the total (i.e., resolved plus SGS) fluxes. A detailed discussion is given in Sullivan et al. (1996). However, this is more difficult to implement. Moreover, toward the top of the relaxation zone at the grid interface, the SGS flux in the nested grid is close to that on the parent grid. This lends some justification to enforcing the conservation condition on the resolved rather than the total vertical fluxes.

The 1D form of the conservation of vertical fluxes in Eq. (4) is expressed as follows:

$$\delta_x \sum_i w'_i \phi'_i = \Delta_x \sum_I W'_I \Phi'_I. \quad (5)$$

If we choose to interpolate the vertical velocity w from W using Eq. (3), rearranging the summation on the left-hand side of Eq. (5), we arrive at

$$\sum_I \left[\sum_{\varepsilon=-(R_x-1)/2R_x}^{(R_x-1)/2R_x} (E_-^{\varepsilon} W'_{I-1} + E_0^{\varepsilon} W'_I + E_+^{\varepsilon} W'_{I+1}) g(\Phi) \right] = R_x \sum_I W'_I \Phi'_I, \tag{6}$$

where ϕ is replaced by its interpolation equation $g(\Phi)$. To satisfy Eq. (6), the interpolation formula $g(\Phi)$ cannot use the same second-order scheme in Eq. (3). One solution that satisfies Eq. (6) is a zeroth-order interpolation:

$$\phi'_i = g(\Phi) = \Phi'_I, \tag{7}$$

where the nested grid directly takes the value of the nearest coarse-grid point. In the model, the zeroth-order interpolation $\phi_{ij} = \Phi_{II}$ is applied in two dimensions and to all other variables except w , where ϕ_{ij} is within the (R_x, R_y) point stencil centered around Φ_{II} .

With the choice of the interpolation formulas in Eqs. (3) and (7), the conservation condition of Eq. (4) is satisfied by all second-order vertical fluxes except the vertical fluxes of vertical velocity $\langle w'w' \rangle$. Moreover, third- and higher-order vertical fluxes (e.g., the vertical flux of the vertical velocity variance $\langle w'w'^2 \rangle$) are not conserved either. The effects of such nonconservation appear small. In the nested simulations, no obvious discontinuities are found in the second-order flux $\langle w'w' \rangle$ and the third-order skewness $S_w = (\langle w'^3 \rangle) / (\langle w'^2 \rangle^{3/2})$, presented later (see Fig. 6 below).

If horizontal nesting is applied, step 5 also interpolates the lateral boundary conditions from the coarse to the fine grid. In this work, the lateral boundaries of the parent and nest domains overlap. Identical lateral boundary conditions are applied to both domains.

4) STEPS 6–8

After boundary conditions are obtained from steps 3 and 5, the nest domain is advanced R times with large time steps $\delta t = \Delta t / R$, where $R = \max(R_x, R_y)$ and $R_{x,y} = \Delta_{x,y} / \delta_{x,y}$ are the nesting ratios in the x and y directions. The time integration for the nested grid is almost the same as that used by the parent grid except for a few changes. In step 6, an additional forcing term $\partial \phi / \partial t_{rf}$, where the subscript rf stands for relaxation forcing, is computed following Harris and Durran (2010):

$$\frac{\partial \phi}{\partial t} \Big|_{rf} = w_{1n} (\phi_c - \phi_n) - w_{2n} \frac{\partial^2 (\phi_c - \phi_n)}{\partial z^2}, \tag{8}$$

where ϕ is a prognostic variable, n is the index of this grid point in the relaxation zone (counting downward from the interpolated point), and ϕ_c is obtained by linearly interpolating in time the coarse-grid

spatially interpolated data from step 5. The weighting coefficients are

$$w_{1n} = \frac{W}{\delta t} \frac{1 + n_{tz} - n}{n_{tz}}, \text{ for } n = 1, 2, \dots, n_{tz}$$

$$w_{2n} = 0.2w_{1n}, \tag{9}$$

where the n_{tz} is the number of vertical levels in the relaxation zone introduced in section 2a. In this study, $n_{tz} = 5$. The coefficient W is set to 0.1 following Harris and Durran (2010). Equations (8) and (9), as well as the value of W , are the same as those used in WRF (Skamarock et al. 2008) except that, in WRF the relaxation zone is in the horizontal directions, and the vertical diffusion term on the right-hand side of Eq. (8) is replaced by horizontal diffusion. The relaxation forcing term is not applied to the turbulent kinetic energy (TKE) because it is grid dependent; a directly interpolated value from the coarse grid is inappropriate for use on the nested fine grid.

The small time steps for acoustic waves are also decreased proportionally by R times $\delta \tau = \Delta \tau / R$. Within the small step, the vertical velocity w and pressure p are solved implicitly (see Xue et al. 2000, appendix B). The top boundary conditions for w and p in the nest domain top are replaced with those obtained from step 5. The exact top boundary values at each small time step for the nested domain from $t - \delta t$ to $t + \Delta t$ are linearly interpolated in time from those obtained at $t - \Delta t$, t , and $t + \Delta t$ from the coarse grid.

5) STEP 9

When the nest domain is integrated up to $t + \Delta t$, its variables are averaged back to the parent grid. This is termed ‘‘anterpolation’’ by Sullivan et al. (1996). Following Harris and Durran (2010), nested grid variables within the relaxation zone are not included in the anterpolation. Anterpolation adopts the averaging formula of Kurihara et al. (1979):

$$\Phi_{II} = \frac{1}{R_x R_y} \sum_i \sum_j \phi_{ij},$$

$$U_{II} = \frac{1}{R_y} \sum_j u_{ij}, \text{ and} \tag{10}$$

$$V_{II} = \frac{1}{R_x} \sum_i v_{ij},$$

where ϕ and Φ represent vertical velocity and all other scalar variables, and U and V are averaged along their cross directions to ensure the conservation of mass fluxes across the lateral walls of each coarse-grid cell. On

the ARPS grid, where a ghost point resides outside the physical domain, i is related to I by (same for j to J)

$$\begin{aligned} i &= R_x I - \frac{3}{2}(R_x - 1), \quad \text{cell center points} \\ i &= R_x I - 2(R_x - 1), \quad \text{cell face points} \end{aligned} \quad (11)$$

depending on whether the variable is located on the cell face, such as u and v , or cell center, such as w and scalars. The summations are operated over the stencil $[i - (R_x - 1)/2, i + (R_x - 1)/2]$ and $[j - (R_y - 1)/2, j + (R_y - 1)/2]$. Special care is taken when antinterpolating higher-order tensors (e.g., the TKE) from the nested grid (Sullivan et al. 1996). In addition to averaging the SGS components, additional TKE, which is resolved on the fine nested grid, but is of subgrid scale on the coarse parent grid must also be accounted for according to

$$\begin{aligned} E_{II} &= \frac{1}{R_x R_y} \sum_i \sum_j e_{ij} + \frac{1}{2} \left[\frac{1}{R_x R_y} \sum_i \sum_j (u_{ij}^2 + v_{ij}^2 + w_{ij}^2) \right] \\ &\quad - \frac{1}{2} (U_{II}^2 + V_{II}^2 + W_{II}^2). \end{aligned} \quad (12)$$

However, according to Eq. (10), U and V are obtained by averaging on their respective cross directions. This means that the $\langle U \rangle$ is not necessarily equal to $\langle u \rangle$, likewise for $\langle V \rangle$ and $\langle v \rangle$. Such inequality can generate an overall bias on the antinterpolated E_{II} . Therefore, an additional term $(1/2)(\langle U \rangle^2 - \langle u \rangle^2 + \langle V \rangle^2 - \langle v \rangle^2)$ is added on the right-hand side of Eq. (12) to correct for this bias.

3. SGS turbulence parameterization

On the parent grid, a PBL scheme is adopted for SGS turbulence parameterization. PBL schemes can be grossly categorized as first- and higher-order schemes. Regardless of the order, the basic formulation of many PBL schemes consists of a gradient diffusion and a countergradient term for the CBL. Take the Troen and Mahrt (1986) model for the SGS heat flux as an example:

$$\overline{w\theta}^{\text{SGS}} = -K_h \left(\frac{\partial \bar{\theta}}{\partial z} - \gamma \right), \quad (13)$$

where K_h is the eddy viscosity for heat, $\gamma \sim \overline{w'\theta'_s}/(w_s z_i)$ is the counter gradient term, $\overline{w'\theta'_s}$ is the surface heat flux, and $w_s = (u_*^3 + 7\epsilon\kappa w_*^3)^{1/3}$ is a surface velocity scale, which is a combination of the friction velocity $u_* = (\overline{u'w_s'^2} + \overline{v'w_s'^2})^{1/4}$ and the convective velocity $w_* = [(g/\Theta_0)\overline{w'\theta'_s z_i}]^{1/3}$. Here, $\overline{u'w_s'}$ and $\overline{v'w_s'}$ are the surface momentum fluxes, ϵ is the dimensionless height of the surface layer, and κ is the von Kármán constant. First-order PBL schemes such as the Yonsei University (YSU) scheme (Hong et al. 2006) parameterize K_h as

$$K_h(z) \sim \kappa w_s z \left(1 - \frac{z}{z_i} \right)^p. \quad (14)$$

Higher-order PBL schemes such as the Bougeault and Lacarrere (1989; BouLac) scheme parameterize K_h through TKE E :

$$K_h(z) \sim \sqrt{E(z)} l_v(z), \quad (15)$$

where E is computed through a prognostic TKE equation, and l_v is a vertical mixing length.

In the grid-refinement-based approach, the unstable surface layer is resolved on a fine nested grid; hence, the appropriate SGS parameterization is an LES-type turbulence closure. Like PBL schemes, LES closures also include first- and higher-order formulations. Example of a first-order closure is the Smagorinsky (Lilly 1967) model. In a vertical model column,

$$K_h(\Delta, z) = C_s \Delta^2 |S(z)|, \quad (16)$$

where S is the strain rate tensor, C_s is the Smagorinsky constant, and $\Delta = (\Delta_x \Delta_y \Delta_z)^{1/3}$ is a grid scale. Example of a higher-order closure is the 1.5-order TKE model of Deardorff (1974):

$$K_h(\Delta, z) = 0.1 \sqrt{E}(\Delta, z) \Delta. \quad (17)$$

When choosing LES closures for the nested grid, it is desirable to pick one whose order is consistent with that of the PBL scheme, which makes it easier for setting boundary conditions for prognostic variables across the grid interface. If inconsistent orders of schemes are used, for example, either a first-order PBL scheme with a 1.5-order LES closure or a 1.5-order PBL scheme with a first-order LES closure, setting boundary conditions for TKE at the grid interface becomes difficult because of the lack of TKE as a prognostic variable on one side of the nest. Although setting an arbitrary zero-gradient boundary condition for TKE is possible, as is done for lateral grid nesting practices, it is unphysical for vertical nests given the relatively large vertical gradients of TKE within the PBL. In this study, both 1.5-order SGS schemes are used. The boundary conditions of TKE across the grid interface are set according to Eq. (12). The relaxation forcing, however, is not applied to TKE because of the difficulties in setting a grid-dependent E_c in Eq. (8).

Besides consistency considerations, an additional reason for favoring higher-order parameterizations is because of the design of the PBL schemes. Traditional PBL schemes are designed to operate on a vertical

model column and are unaware of the horizontal grid spacing Δ . For example, according to the expression of K_h in Eq. (14), the velocity scale w_s is determined by surface fluxes, while the length scale varies as a polynomial function of height. Given the same vertical gradient $\partial\bar{\theta}/\partial z$ and surface fluxes, a first-order PBL scheme in the form of Eq. (13) predicts the same amount of SGS fluxes regardless of Δ , whereas the SGS fluxes should decrease as Δ is refined (Honnert et al. 2011; Shin and Hong 2013). Such insensitivity to Δ is one of the fundamental barriers that prevent the direct application of PBL schemes on a gray-zone grid.

In the grid nested setup, convection is explicitly resolved in the nested grid and antepolated back to the parent grid. As the parent grid falls inside the gray zone, the antepolated fluxes are partially resolved and nonnegligible. Since the SGS fluxes from the PBL scheme are grid insensitive, adding a non-zero amount of resolved fluxes (because of antepolation) can lead to an overprediction of the total fluxes. The same problem, known as double counting of fluxes (e.g., Xue et al. 1996), occurs when applying PBL schemes to fine, convection-resolving grids. The erroneous heat fluxes can lead to changes in the mean state of $\bar{\theta}$ and even result in a slightly stable profile ($\partial\bar{\theta}/\partial z > 0$). This in turn leads to a different formulation of K_h for stable conditions. The SGS gradient diffusion flux ($K_h \partial\bar{\theta}/\partial z$) in the PBL scheme [first part of Eq. (13)] then adjusts because of the changes in both the vertical gradient and the eddy diffusivity.

Traditional higher-order PBL schemes are also grid unaware by design. Higher-order moments, such as TKE in Eq. (15), are also solved along a vertical model column. However, their reliance on higher-order moments provides a means of adaptation to scale- or grid-aware formulations. For example, when a 1.5-order TKE closure is used in the LES grid, the predicted TKE is certainly grid aware. When antepolated back to the parent grid, additional fluxes of resolved scale to the nest but of subgrid scale to the parent grid are also added [see Eq. (12)]. This builds in grid awareness to the parent grid TKE, and in turn, the eddy diffusivity K_h in Eq. (15) also becomes grid aware through \sqrt{E} . In theory, this is a smoother grid-aware adaptation of PBL schemes rather than the adjustment of mean profile mechanisms in first-order schemes.

In this study, both the PBL scheme and the LES closure use a 1.5-order TKE formulation. Following Xue et al. (1996), the PBL scheme of Sun and Chang (1986; SC) is used for vertical mixing. Mixing length l_v in Eq. (15) is diagnosed as

$$l_v = 0.25 \left\{ 1.8z_i \left[1 - \exp\left(-4\frac{z}{z_i}\right) - 0.0003 \exp\left(8\frac{z}{z_i}\right) \right] \right\}, \quad (18)$$

where $4l_v$ is the empirically derived peak spectral wavelength of the vertical velocity by Caughey and Palmer (1979). The coefficient 0.25 is optimally tuned for the Wangara test case. The LES closure is the Deardorff 1.5-order TKE model in Eq. (17). The combination of YSU as the PBL scheme and Smagorinsky as the LES closure is also tested. Results are qualitatively similar (not shown in this study); the vertical temperature profile does become more stable in the mixed layer in the nested simulation, because of the mean profile adjustment mechanism. The adjustment of PBL schemes to grid spacing is explored in Shin and Dudhia (2016).

4. Simulation setup

The test case is based on the well-studied Australian Wangara Experiment (Clarke et al. 1971). It describes a time-evolving CBL from 0900 to 1800 LST for day 33 (16 August 1967) of the experiment. The case setup follows Yamada and Mellor (1975) and is not repeated here for brevity. All simulations are performed on a $36 \text{ km} \times 36 \text{ km} \times 2.5 \text{ km}$ domain. A list of key model parameters is presented in Table 1. A 50-m stand-alone high-resolution LES (SA50) is performed to serve as a benchmark ‘‘truth’’¹ for the Wangara CBL. The 900-m stand-alone simulation (SA900) is used as the control simulation. All simulations have 50 vertical levels with uniform Δz of 50 m, except for the nested 180-m run with six nest levels and a stretched vertical grid (N180-L6-S), where a vertically stretched grid is used to test the effects of grid stretching with nesting. The stretched grid has 25 vertical levels, with an average Δz of 100 m and a minimum Δz of 50 m near the surface.

Nested simulations are performed on varying horizontal grid spacing $\delta_{x,y}$ and vertical levels of nest n_z . Two $\delta_{x,y}$ (180 and 100 m) are used following 5:1 and 9:1 nesting ratios. Conventionally, 3:1 and 5:1 ratios are used (Zhong and Chow 2012), although higher ratios have been reported [e.g., 10:1 in Zhou and Chow (2013) and 11:1 in Muñoz-Esparza et al. (2017)]. The major issue associated with large nesting ratios is the elongated transition fetch from the coarse to the fine grid (Muñoz-Esparza et al. 2014). However, this issue does not seem

¹ Zhou et al. (2014) showed that the Wangara CBL is well resolved at 50-m isotropic spacing, where higher-order statistics and spectra have converged.

TABLE 1. List of model parameters. Stand-alone and nested simulations are denoted by “SA” and “N” in the run names; “S” and “LF” at the end of the run names stand for stretched vertical grid and locally computed fluxes on the nest domain, respectively. Parent and nest variables are distinguished by capital and small letters. Nested simulations are named by their respective grid spacing on the nested grid followed by the vertical levels of the nest. The five-point sponge zone is not counted in the vertical nest level n_z , since variables in the sponge zone are not antepolated. Ghost points are excluded in the number of grid points.

Run name	$\Delta_{x,y}(\delta_{x,y})$ (m)	$N_{x,y}(n_{x,y})$	$N_z(n_z)$	Δz (m)
SA50	50	720	50 (—)	50
SA100	100	360	50 (—)	50
SA180	180	200	50 (—)	50
SA900	900	40	50 (—)	50
N100-L6	900 (100)	40 (360)	50 (6)	50
N100-L16	900 (100)	40 (360)	50 (16)	50
N180-L6	900 (180)	40 (200)	50 (6)	50
N180-L16	900 (180)	40 (200)	50 (16)	50
N180-L6-S	900 (180)	40 (200)	25 (6)	100
N180-L6-LF	900 (180)	40 (200)	50 (6)	50

to be present in our vertical nest setup for the 9:1 nested simulation (see Fig. 8 and discussion). On the other hand, coarser $\delta_{x,y}$ are not used to avoid the gray zone on the nest grid, which extends to 400-m grid spacing as shown in Zhou et al. (2014). Given an approximate upper limit for the fine nest grid spacing of 400 m, and following a conventional upper limit for the nesting ratio of 5:1, the parent grid spacing should not exceed 2 km in practice. This is a practical limitation for the method considering that the CBL gray zone typically begins at 4 km (Gibbs et al. 2011). A nested simulation with 1.8-km grid spacing on the parent domain and 360-m spacing on the nest domain (i.e., a 5:1 nesting ratio) is also tested (results not shown). The nested run develops resolved convection early on, whereas the stand-alone 1.8-km run initiates spurious resolved convection past 1400 LST. However, the simulated convective circulations are too strong compared to the LES results, suggesting contamination from the 1.8-km parent grid. This issue will be discussed in section 5. Finally, a five-point sponge zone at the top of the nest domain is used for all nested simulations. Preliminary tests of a shallower three-point sponge zone leads to kinks in the higher-order profiles and is therefore not used.

5. Results and discussion

a. Mean profiles and onset of resolved convection

Figure 3 presents the vertical profiles of horizontally averaged potential temperature $\langle \Theta \rangle$ of the SA50 and SA900 runs, and the nested 180-m run with six nest levels (N180-L6). Details of the simulation setup are

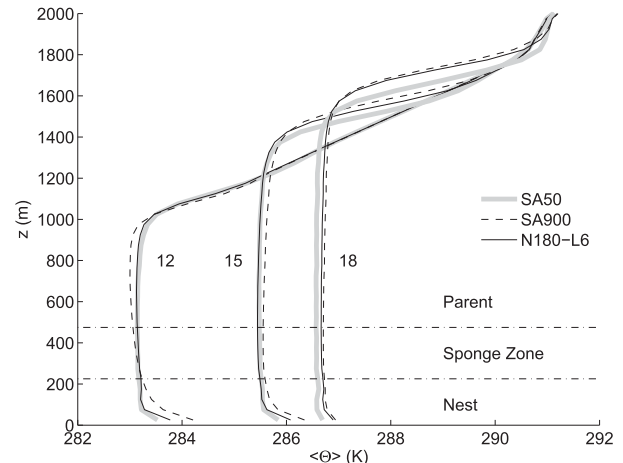


FIG. 3. Comparison of horizontally averaged potential temperature at 1200, 1500, and 1800 LST.

given in Table 1. The $\langle \rangle$ stands for horizontal averaging. Profiles from other nested runs are not shown since they are close to the N180-L6 run. Vertical dashed lines indicate the respective heights of the top of the nest and the sponge zone. Both the SA900 and the N180-L6 profiles agree quite well with the SA50 benchmark, especially at later times and in the nested run. The same can be observed for $\langle u \rangle$ and $\langle v \rangle$ (not shown). Another important first-order variable, the boundary layer depth $\langle z_i \rangle$, is presented in Fig. 4; z_i is diagnosed as the elevated level of neutral buoyancy for a surface parcel. Good agreement with SA50 is also achieved for both the stand-alone and nested simulations for $\langle z_i \rangle$. The agreement of first-order statistics is expected. They should converge as long as there exists sufficient turbulent mixing to produce a well-mixed first-order profile, regardless of whether mixing is from explicit resolution in SA50 or SGS transport in SA900 or a mixture of both in N180-L6.

Despite the overall agreement, $\langle \Theta \rangle$ of SA900 at 1200 LST is slightly superadiabatic throughout the depth of the CBL (Fig. 3), while that of SA50 is very close to neutral between the surface layer and the CBL top. The surface temperature of SA900 is also warmer than the other two by about 0.3 K. During the entire simulation, $\langle z_i \rangle$ is deeper in SA900 than SA50, by as much as about 100 m at 1800 LST (see also Fig. 4), mainly because of the warmer surface temperature. This is due to the PBL scheme being insufficient near the surface (Xue et al. 1996), so a stronger vertical temperature gradient results because of the accumulation of heat in the surface layers. In comparison, the N180-L6 profile is improved through nesting, especially at 1200 LST. This is because the unstable surface layer is explicitly resolved by the nested grid early on in the simulation, therefore producing sufficient mixing for the surface layer.

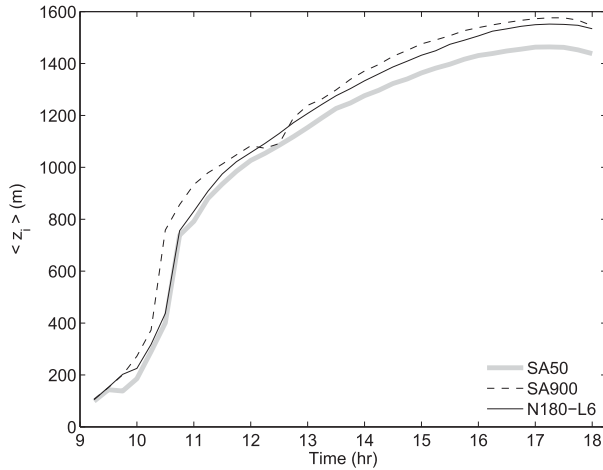


FIG. 4. Time series of horizontally averaged boundary layer depth. Data shown every 900 s.

To show the onset timing of explicit convection, time–height contours of $\langle w'w' \rangle$ calculated from the model-resolved w are presented in Fig. 5. Both N180-L6 and N180 with 16 nest levels (N180-L16) are presented alongside SA900, while SA50 is presented as a benchmark. An arbitrary value of $1 \times 10^{-4} \text{ m}^2 \text{ s}^{-2}$ is picked as a threshold indicator for the onset of resolved convection, as marked by the leftmost contour level in Fig. 5. For SA900, the onset time is around 1100 LST, while vigorous convection does not occur until 1200 LST. In comparison, both nested simulations (Figs. 5b and 5c) show resolved convection a little before 1000 LST in the surface layer, in agreement with SA50 in Fig. 5d. The $1 \times 10^{-4} \text{ m}^2 \text{ s}^{-2}$ contours are positively slanted, indicating that explicit convection at a higher elevation is observed at successively later times. This agrees with the surface-layer initiation of instability and the subsequent upward propagation presented in Zhou et al. (2017). The onset of convection is similar between the two nested runs despite different nest levels. This suggests that the initial surface layer instability is resolved with six levels of nests. Increasing the nest level does not affect the onset timing of convection much.

In Fig. 5a, between 1200 and 1300 LST, a strong patch of $\langle w'w' \rangle$ is found in SA900. This is due to a near-pulse-type release of the accumulated heat/thermal instability (see profile of $\langle \Theta \rangle$ at 1200 LST in Fig. 3) with the onset of explicit convection in SA900. A sign of this sudden release of instability is also evident in the dip of z_i around the same time in Fig. 4, because of the reduced surface temperature and, therefore, the diagnosed z_i . In comparison, the contours of $\langle w'w' \rangle$ vary smoothly in the nested runs, since convection is explicitly resolved in the surface layer, so that surface heat is continuously and

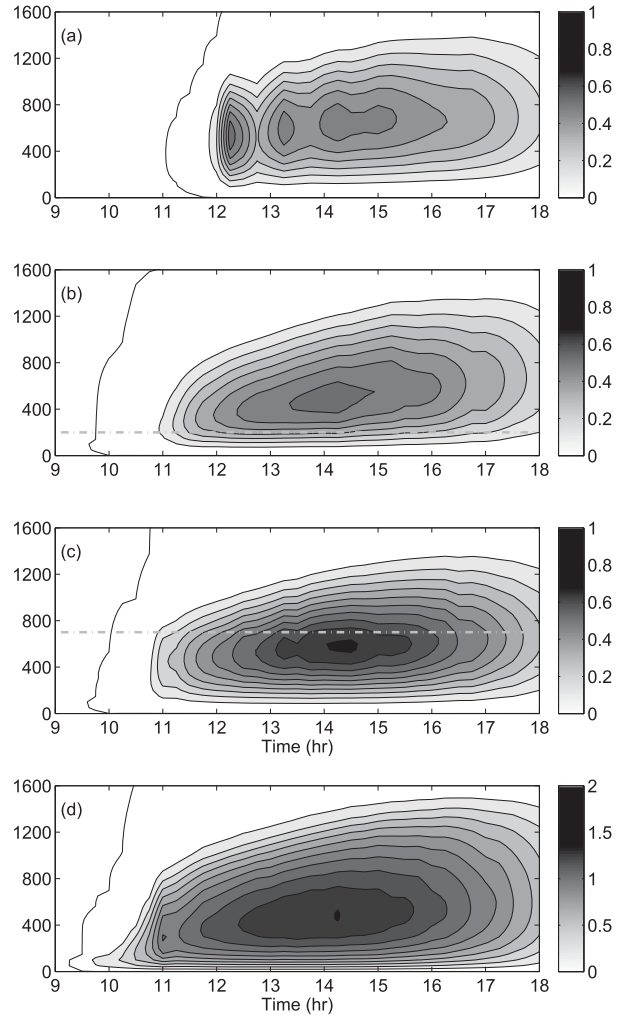


FIG. 5. Time–height contours of $\langle w'w' \rangle$ from (a) SA900, (b) N180-L6, (c) N180-L16, and (d) SA50. Contour interval is $0.1 \text{ m}^2 \text{ s}^{-2}$ except for the leftmost contour, which is at $1 \times 10^{-4} \text{ m}^2 \text{ s}^{-2}$. The horizontal dashed lines mark the respective level of nest.

efficiently transported upward. Finally, the magnitude of $\langle w'w' \rangle$ is sensitive to the level of nests. With a deeper nest, the flow is better resolved to higher levels, resulting in larger $\langle w'w' \rangle$ for N180-L16.

To better compare $\langle w'w' \rangle$, along with other higher-order statistics, their horizontally averaged vertical profiles are plotted in Fig. 6. Instead of SA50, the filtered SA50 results are presented to provide direct comparison among simulations. The filtered data are obtained by spectral filtering of SA50 to remove wavelengths smaller than $2 \times 900 \text{ m}$ so as to represent the true resolved flow statistics on the gray-zone grid. The time presented is at 1500 LST, when vigorous resolved convection is achieved for all simulations. At 1200 LST, turbulent mixing is mostly done by the PBL scheme for the SA900

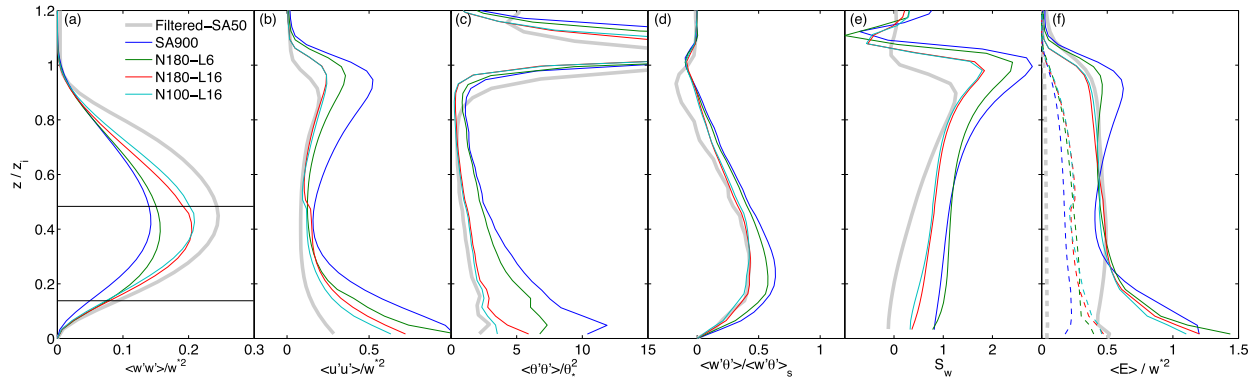


FIG. 6. Horizontally averaged resolved (a) w variance, (b) u variance, (c) θ variance, (d) sensible heat flux, and (e) skewness of the vertical velocity at 1500 LST. Variances are normalized by w^* and $\theta_*^2 = (\overline{w'\theta'_s}/w^*)^2$. Sensible heat flux is normalized by its surface values $\overline{w'\theta'_s}$. The horizontal dashed lines mark 6 and 16 levels of nest. In (f), solid and dashed lines represent the total and the SGS TKE, respectively.

run; hence, resolved higher-order statistics are small because of the absence of resolved convection.

In Fig. 6, SA900 produces the smallest variance profile of $\langle w'w' \rangle$. Note that this is not due to normalization by a different w^* , which is very similar in magnitude among all simulations (not shown). In comparison, N180-L6's w variance is slightly larger and closer to the benchmark profile of the filtered SA50. Increase in the nest domain height to about $z/z_i \sim 0.5$ in N180-L16 enlarges $\langle w'w' \rangle$ between 0.4 and $0.8z/z_i$. Further refinement of the grid spacing of the nest domain to 100 m only shows very small changes [nested 100-m run with 16 nest levels (N100-L16)], indicating the convergence of profiles. The increase of $\langle w'w' \rangle$ from SA900 to N180-L6 suggests that convective eddies in the scale range of 140–900 m, which is roughly $0.2\text{--}0.5z_i$ for a 1400-m-deep CBL, are important for the development of organized convection. As Hunt et al. (1988) laid out, organized convection (which they referred to as thermals) gains strength as the thermals rise by merging small turbulent eddies (plumes). When the surface layer is refined through nesting, small plumes are better resolved. Consequently, thermals can feed on their energy and invigorate, leading to larger $\langle w'w' \rangle$ on the parent grid. Plume-merging processes are not only essential in the surface layer, where small-scale plumes are omnipresent, but are also important in the lower mixed layer (Hunt et al. 1988). This could explain the further increase in $\langle w'w' \rangle$ on the parent grid when the nesting level is raised in N180-L16. The slight differences between N180-L16 and N100-L16 suggest that convective eddies of scales smaller than $0.2z_i$ do not contribute much to thermals. This is supported by Sullivan et al. (1996), where they found small-scale surface layer plumes have minor effects on the mixed-layer dynamics.

Figures 5 and 6a together suggest that organized convection initiates in the unstable surface layer. As thermals ascend into the mixed layer, they continue to gain strength by merging smaller plumes. If the nest domain is limited to the surface layer only, as in N180-L6, the onset and the initial structure of organized convection is improved. But to optimally nurture the growth of thermals above the surface layer, the nest domain should extend to the lower half of the mixed layer. But even so, the nested simulations still do not solely determine the characteristics of convection in the CBL. As evidenced in Fig. 6a, the maximum $\langle w'w' \rangle$ in all nested simulations occur at a slightly lower height compared to the filtered SA50. This points to the deficiencies of the PBL scheme on the parent grid that affect the overall $\langle w'w' \rangle$ profiles.

The vertical profiles of $\langle u'u' \rangle$ in Fig. 6b and skewness S_w in Fig. 6e further reveal contamination due to the PBL scheme on the parent gray-zone grid. For both statistics, the N180-L6 profiles show slight improvements over the original SA900 profiles. More significant improvements are observed for a deeper nest (N180-L16). Further increase of the nest resolution results in only modest changes in the vertical profiles compared to the coarser nest. Note that even at N100-L16, the resulting profiles are still different from the filtered SA50 run. This is clearly observed in the profiles of $\langle u'u' \rangle$ and S_w below $0.5z_i$. The cause of such disagreement is likely due to the limitations imposed by the 900-m resolution of the parent grid. As will be shown later (in Fig. 9), the 900-m parent grid still influences the overall simulation even in the nested region, although the magnitude of the gray-zone effects due to the 900-m grid are reduced.

Profiles of $\langle \theta' \theta' \rangle$ in Fig. 6c show improvements in the nest simulation N180-L6 compared to the stand-alone gray-zone run SA900, although the variance is still overestimated compared to the LES benchmark. Further increase of the nest level to 16 reduces $\langle \theta' \theta' \rangle$ and brings the overall profile closer to that of the filtered SA50. Increasing the resolution to 100 m in the nest domain results only in a small reduction of $\langle \theta' \theta' \rangle$, consistent with other second- and third-order profiles in Fig. 6. The resolved heat flux $\langle w' \theta' \rangle$ profiles in Fig. 6d show the largest improvement from N180-L6 to N180-L16. Nevertheless, the resolved heat flux is still overestimated in the finest-resolution run with the highest nest domain height N100-L16. The overestimation of the heat flux in the nested surface layer is likely due to the overestimation of $\langle \theta' \theta' \rangle$.

The total and the SGS components of TKE are presented in Fig. 6f alongside the resolved components in Figs. 6a and 6b. The total and the SGS TKE profiles from SA50 rather than filtered SA50 are plotted for direct comparison. Compared to SA50, all other runs overpredict the total TKE below $\sim 0.3z/z_i$, regardless of the nesting configurations. The overprediction is mainly due to the resolved horizontal components of TKE presented in Fig. 6b. Above $0.3z/z_i$, better agreements with SA50 are achieved for the nested runs compared to the stand-alone 900-m run. While some underprediction of total TKE is found in N180-L6 between 0.3 and $0.8z/z_i$, the vertical profiles of N180-L16 and N100-L16 nearly overlap with that of SA50. The SGS TKE e in the nested runs shows interesting features. Most notably in N180-L16 and N100-L16, an increase of e is observed above $\sim 0.5z/z_i$, which is right outside the nest domain. The increase in e compensates for the decrease in the horizontal component of the resolved TKE as seen in Fig. 6b, such that the total TKE is smooth over the nest grid interface. Overall, e is larger in the nested runs than SA900.

Once resolved convection emerges, overshooting thermals contribute to the entrainment of the free tropospheric air. To investigate the effects of nesting on the entrainment flux, the entrainment flux ratio R_H is presented in Fig. 7, where R_H is defined as the ratio of the entrainment flux to the surface flux of heat (Holtslag and Moeng 1991). Here, heat fluxes include both resolved and SGS contributions; R_H from the LES benchmark increases with time, with a value slightly less than 0.2 for the most of the day. Such values are within the expected ranges of CBL entrainment (Gentine et al. 2015). For SA900, R_H is underestimated at 1000 and 1100 LST, which means the entrainment fluxes are underestimated, since the surface flux is imposed as a boundary condition. At 1200 LST, R_H of the SA900 run rapidly

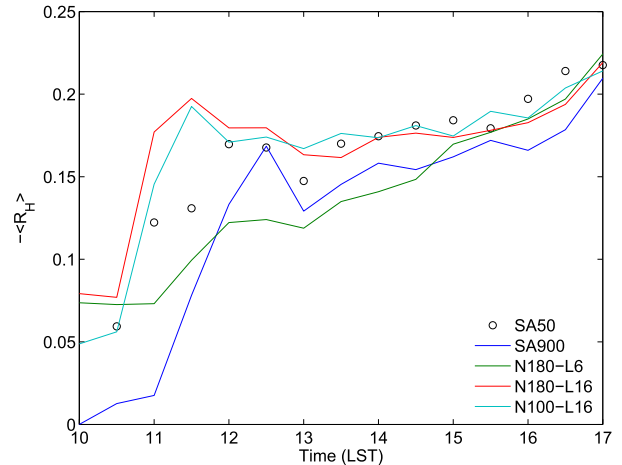


FIG. 7. Time series of the horizontally averaged entrainment flux ratio R_H .

increases, which corresponds to the onset timing of spurious convection on the 900-m grid (see Fig. 5a). The underprediction of the entrainment flux on gray-zone grids at the morning transition was also noted in Efstathiou et al. (2016). In comparison, R_H from N180-L6 is closer to the LES benchmark. This is a result of the nested simulation's ability to resolve organized convection early on in the simulations. The magnitude of the entrainment fluxes is still less than the LES benchmark, suggesting that thermals from a six-level nest are not strong enough. This is also evidenced in the discussion of $\langle w' w' \rangle$ profiles in Fig. 6a. When the nest levels are raised to 16, allowing plume-merging processes to be better resolved in the lower part of the mixed layer, entrainment fluxes increase further in agreement with the LES benchmark.

b. Flow visualization and spectra

Figure 8 shows the convective structures of the stand-alone gray zone and the two nested simulations in terms of w in the vertical and horizontal cross sections at 1200 LST, the early stage of CBL development. The filtered SA50 contours are also presented as a benchmark in the rightmost column. The contours of the nested simulations are from the parent 900-m grid. As previously shown at 1200 LST, the SA900 run has just reached its onset of resolved convection (see Fig. 5). This is evidenced in the lack of convective structures in the leftmost column of Fig. 8 for the SA900 run. In Figs. 8e, 8i, and 8m, the horizontal convective cells are barely forming. The magnitude of resolved w is about twice as small as in the nested runs at the same time. In comparison, contours of N180-L6 in the second column show much more organized convective structures within

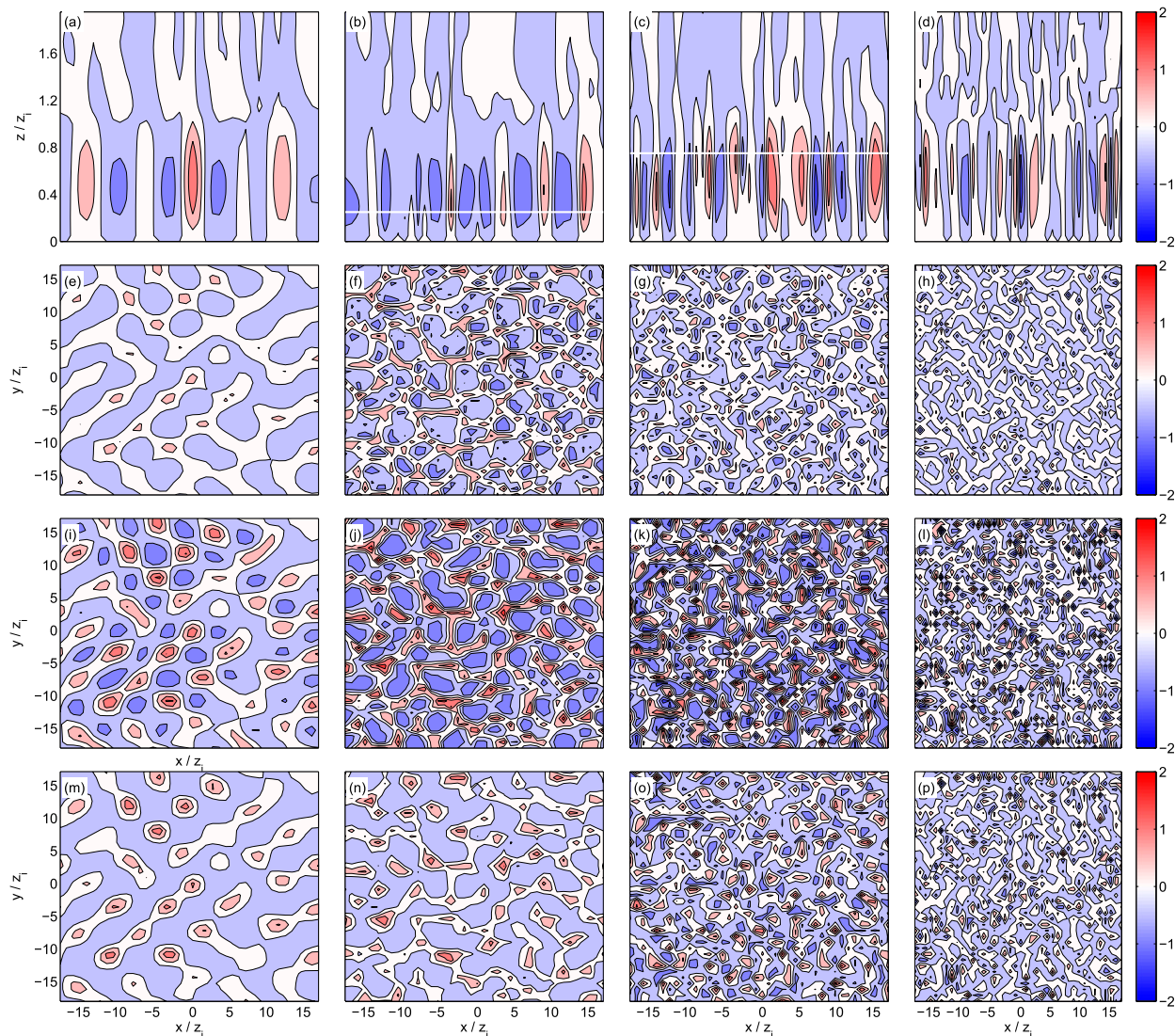


FIG. 8. Contours of w from (a),(e),(i),(m) SA900, (b),(f),(j),(n) N180-L6, (c),(g),(k),(o) N180-L16, and (d),(h),(l),(p) the filtered SA50 at 1200 LST. Here, (a)–(d) are along the x – z vertical cross section at $y = 0$; (e)–(h), (i)–(l), and (m)–(p) are along the horizontal cross sections at $z/z_i = 0.15, 0.5$, and 0.85 , respectively. Contour interval is 0.5 m s^{-1} .

($z/z_i \sim 0.15$; Fig. 8f) and above the nested grid in the mixed layer ($z/z_i \sim 0.5$; Fig. 8j) and in the entrainment zone ($z/z_i \sim 0.85$; Fig. 8n). Contours along the x – z plane in Fig. 8b reveal no apparent discontinuities across the nest interface. The convective structures at $z/z_i \sim 0.5$ strongly mimic that at $z/z_i \sim 0.15$ for N180-L6, with less sharp edges along the spokelike updrafts. This is because convective structures above the nest region are primarily driven by resolved convection inside the nest. In the entrainment zone, only the core of the thermals from the mixed layer is left.

Compared to a 6-level nest, a 16-level nest in the third column reveals even finer-resolved convective structures, which strongly resembles the idealized filtered-LES field in

the last column. The size of the organized vertical convective motions is smaller for N180-L16 than N180-L6, as seen most clearly from the increased number of up- and downdrafts in the vertical cross section in Fig. 8c compared to Fig. 8b. A close comparison of the third and fourth columns, especially Figs. 8k and 8l, reveals that the convective structures on the parent grid of N180-L16 are “too” organized, while the filtered SA90 contours appear more random.

To quantitatively assess the simulated convective structures in Fig. 8, the energy spectra of w' at 1200 LST are presented in Figs. 9a and 9b. The original SA50 spectra are also presented as a reference. Peaks in the energy spectra correspond to wavenumbers where most

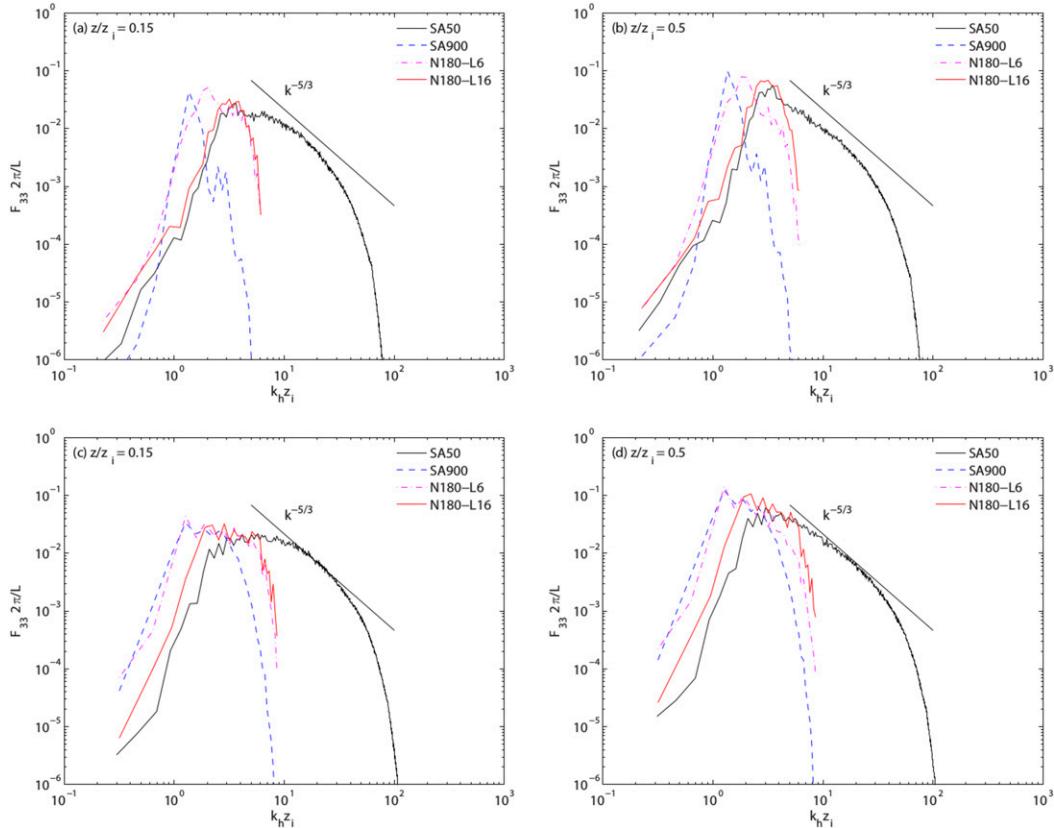


FIG. 9. Horizontal energy spectra of w' at (a),(c) $z/z_i = 0.15$ and (b),(d) $z/z_i = 0.5$ at (top) 1200 and (bottom) 1500 LST; $k_h = \sqrt{k_x^2 + k_y^2}$ is the horizontal wavenumber.

of the energy resides. Physically, they represent the characteristic sizes of the convective cells in Fig. 8 (Kaimal and Finnigan 1994, chapter 2). Spectra at $z/z_i = 0.85$ are not presented since they resemble the spectra at $z/z_i = 0.5$ qualitatively. First, observe that in Figs. 9a and 9b, the SA900 spectra peak at a smaller wavenumber than the nested simulations. This is due to the grid-dependent characteristics of gray-zone convection on the 900-m grid, where the onset of resolved convection is triggered when a grid-dependent critical turbulent Rayleigh number is reached (Zhou et al. 2014). As a result, spurious convection with much wider characteristic scales appears on the gray-zone grid.

At $z/z_i \sim 0.15$ and 0.5 , N180-L16 produces spectra that agree well with the SA50 spectra at the longer-wavelength end. On the high-wavenumber (small wavelength) side, the spectra are expected to drop because of the resolution limit, while on the low-wavenumber (long wavelength) side, the “ideal” coarse-resolution spectrum should overlap the fine-resolution one. A close inspection of the N180-L6 spectra reveals two peaks, most notably in Fig. 9a. Although its shorter-wavelength peak overlaps nicely with that of N180-L16, its spurious longer-wavelength peak has

a slightly larger magnitude than the shorter-wavelength one. Even so, the wavelength of the spurious peak still occurs at a shorter wavelength than the single peak found in SA900. At $0.5z/z_i$, qualitatively similar patterns are found, except that the magnitude of the second peak in N180-L6 is much larger than the high-wavenumber peak, apparently because of the larger influence of the coarse-grid resolution at this level. Toward the high wavenumbers, the spectral energy in N180-L6 is also smaller than N180-L16. But the spectral energy in both nested runs is at least an order of magnitude larger than that of SA900, giving rise to the finer details observed in Fig. 8.

The convective structures are examined again at 1500 LST, when all simulations produce vigorous resolved convection. For SA900 in the first column of Fig. 10, the model domain is filled with large convective cells that resemble real convective structures. In Figs. 10e and 10i, the convective cells are from about 5 to $6z_i$ wide, larger than the $\sim 2z_i$ size predicted by thermal instability theory. The cause of such grid dependency of convective structures is explained in detail in Zhou et al. (2014). Compared to SA900, the N180-L6 contours in the second column produce slightly finer-scale

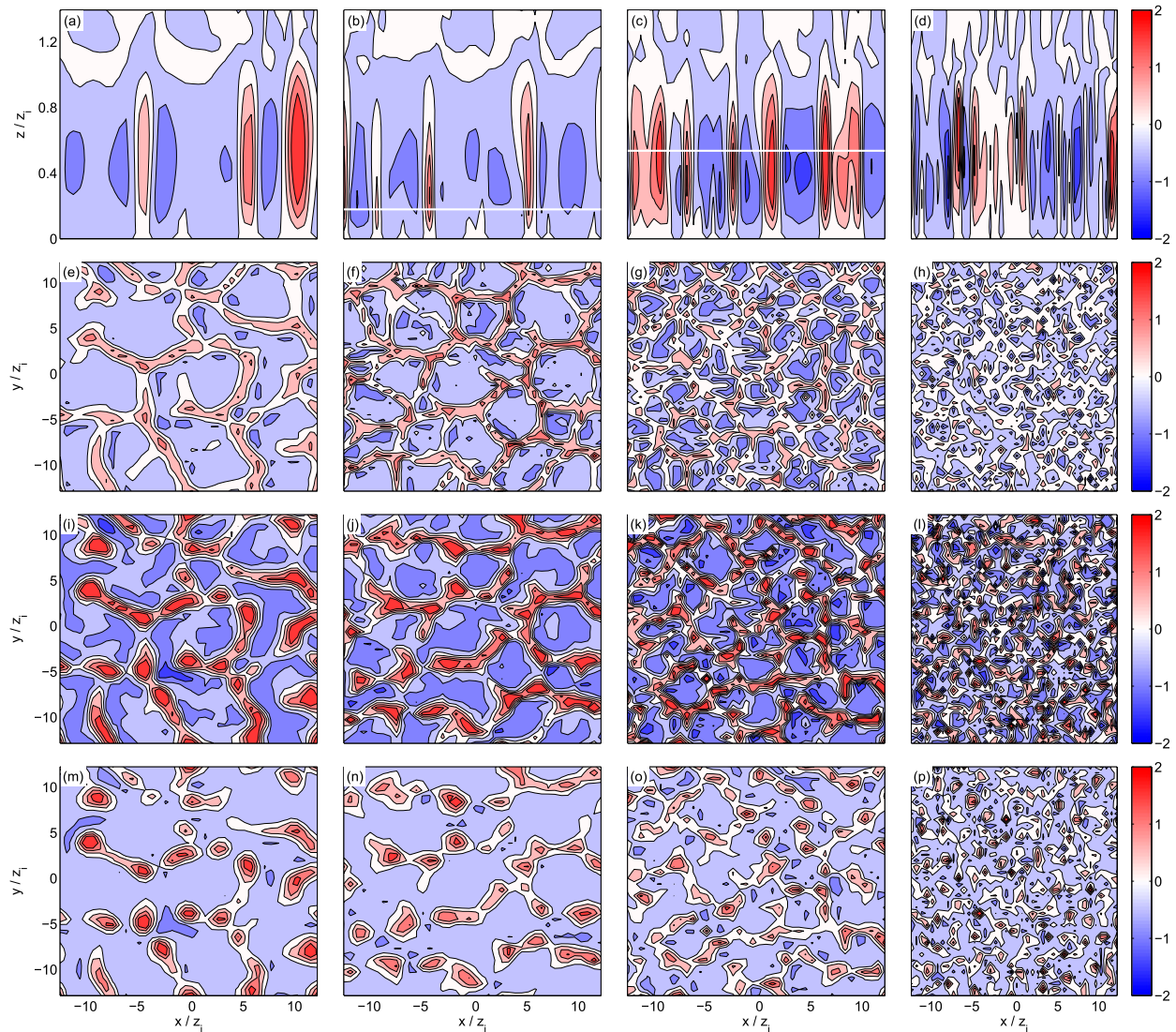


FIG. 10. As in Fig. 8, but at 1500 LST.

convective structures. Despite the similarity in the cell size, the small-scale details are richer in the nested run. For the N180-L16 contours in the third column, the characteristic sizes of the convective cells are markedly smaller. The flow field also includes a rich amount of small-scale details. The filtered-LES benchmark on the rightmost column shows much less organization but more details. Compared with the filtered LES, it is clear that even though nested simulations show successive improvements over the stand-alone gray-zone run, they still fail to simulate the correct convective structures even for N180-L16.

The length scales of convection are again assessed through the energy spectra of w' in Figs. 9c and 9d. At $z/z_i \sim 0.15$ in Fig. 9c, the peak of the SA900 spectrum

occurs again at a small wavenumber, where the spectrum should be decreasing according to the SA50 benchmark. The N180-L16 spectrum peaks at a smaller wavelength around $1.5z_i$. Its peak wavelength and magnitude overlap nicely with the SA50 spectrum. There is an excess of energy on its small-wavenumber side, although not as much as in the SA900 spectrum. The N180-L6 spectrum exhibits a mixed behavior. Its high-wavenumber side closely follows the N180-L16 spectrum, while its low-wavenumber side nearly overlaps that of the SA900 spectrum. A qualitatively similar behavior is also found at $z/z_i \sim 0.5$ in Fig. 9d. The N180-L16 spectrum shows relatively large fluctuations, possibly due to the limited number of grid points (i.e., sample size) for averaging. Overall, the N180-L16 spectrum shows the best

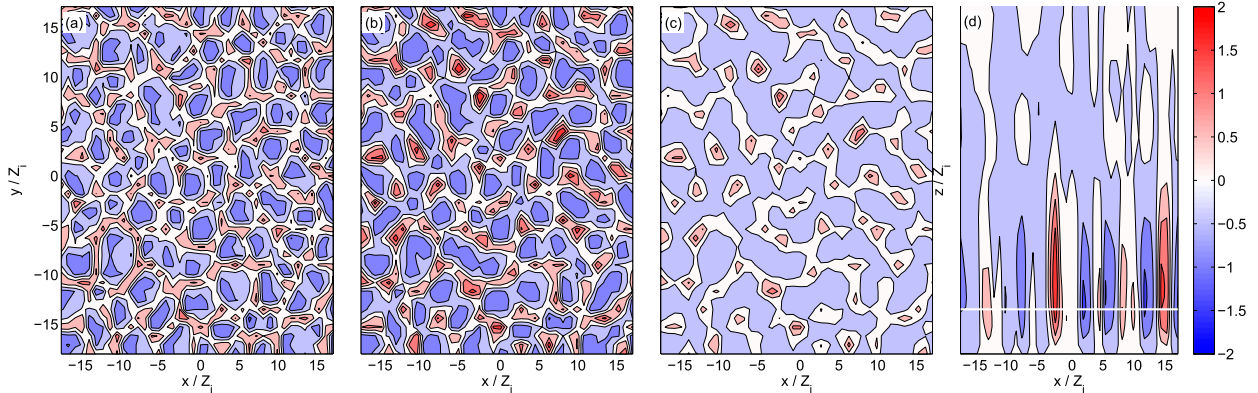


FIG. 11. As in Fig. 8, but for N180-L6-S at 1200 LST.

agreement with SA50. Excessively long wave components dominate the SA900 spectrum. The N180-L6 spectrum falls somewhere in between.

c. Additional tests

Numerical weather prediction (NWP) applications almost always adopt vertical grid stretching to allow for more resolution in the boundary layer. To test the nesting configuration in the presence of vertical grid stretching, an additional run (N180-L6-S; see Table 1) is performed. In N180-L6-S, the vertical grid is stretched using a hyperbolic tangent function, with minimum surface spacing of 50 m and average spacing of 100 m (Xue et al. 1995). The convective structures at 1200 LST are presented in Fig. 11 and are similar to their uniformly spaced counterparts N180-L6 in Fig. 8. In the vertical cross section in Fig. 11d, the vertical convection cells are continuous across the nest interface. First- and higher-order mean profiles are also close to those of N180-L6 (not shown). Overall, the vertical nesting procedure works well under a vertically stretched grid.

Another test (N180-L6-LF; see Table 1) is performed whereby the surface momentum fluxes on the nest grid are computed locally according to Eq. (1) rather than interpolated from the parent grid as is done in section 2b (2). Other aspects of the N180-L6-LF setup are identical to that of N180-L6. Note that the heat flux is prescribed as boundary conditions according to section 4 and is left unchanged. The impact of locally computed momentum fluxes on wind speed is examined first. Time series of wind speed at the first grid point above the surface, where the largest impacts are expected (Moeng et al. 2007), are presented in Fig. 12a. Compared to the control run N180-L6, surface wind speeds are slightly larger when momentum fluxes are computed locally. Although the positive bias largely persists throughout the daytime, its magnitude is quite moderate. More significant changes

are found in the variances of horizontal velocity. The vertical profiles of $\langle u'u' \rangle$ at 1500 LST are presented in Fig. 12b. Larger variances, most prevalent in the surface layer, are found throughout the depth of the CBL when fluxes are computed locally.

To investigate the source of the increased variance, horizontal contours of the perturbation horizontal velocity $u' = u - \langle u \rangle$ are inspected (results not shown). The overall organized patterns are similar between the control run N180-L6 and the local flux run N180-L6-LF. However, N180-L6-LF has more finer-scale details than the control run. Further examination of the horizontal energy spectra reveals that more energy resides in the N180-L6-LF run than the control run at high wavenumbers. Both the control run and local flux run overpredict the peak energy strength compared to the stand-alone LES run. Overall, computing momentum fluxes locally allows finer details to appear in the flow field. This is because more heterogeneity is permitted through locally varying surface fluxes on the fine nest grid, which in turn feeds back to the parent grid. While the mean profiles of wind change slightly, more prevalent increases are observed in the variance profiles, not only near the surface but extending to the entire depth of the CBL. For the current study, computing local momentum fluxes is undesirable, because doing so adds more variance to the already overestimated $\langle u'u' \rangle$ because of the contamination of the spurious convection on the parent grid (see Figs. 6b and 12a).

d. Computational costs

The use of increased resolution within the nested near-surface layer increases computational cost. To give a quantitative assessment, the normalized CPU times of nested runs with horizontal nesting ratios of 5:1 and 9:1 are given in Fig. 13 relative to the CPU time of SA900. The six-level nested simulations are about 50

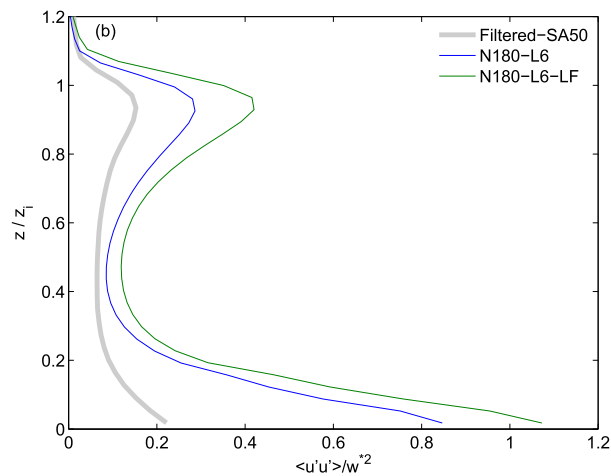
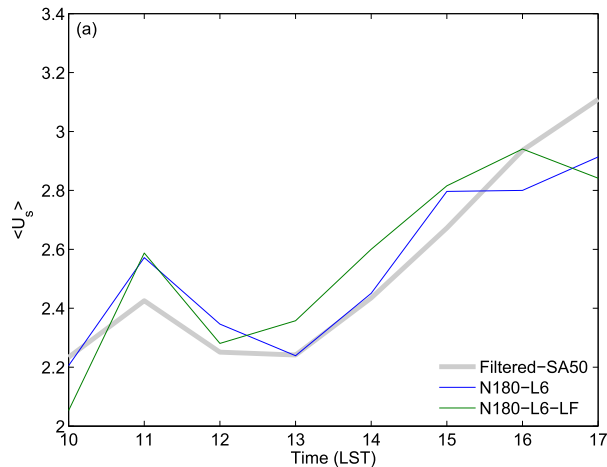


FIG. 12. (a) Time series of horizontally averaged surface wind speed ($\langle U_s \rangle$) and (b) horizontally averaged vertical profiles of $\langle u'u' \rangle$ at 1500 LST.

and 300 times more expensive than SA900 for 5:1 and 9:1 nesting ratios. The 16-level nest is about twice as expensive as the 6-level nest. The added computational expenses are certainly significant. However, compared to running the model at full resolutions, the nested grid approach is still more economical. For the 5:1 nesting ratio, the cost of a nested run is about 70% and 20% cheaper compared to a stand-alone run for 6 and 16 levels of nest, respectively. The savings further increase to about 90% and 85% for a 9:1 nesting ratio.

Note that the code has not been optimized for computational efficiency. For example, we made extensive use of existing ARPS subroutines for the ease of coding. Many variables, such as those related to the land surface module, were defined and carried around without any utility to avoid changes to the existing subroutines.

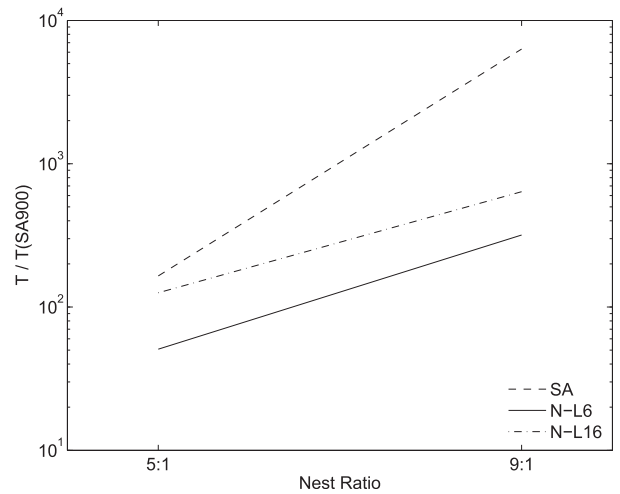


FIG. 13. Normalized CPU time of the stand-alone and nested runs.

Furthermore, when parallel capability was implemented, we used the same processor for the parent subdomain to host the same nest subdomain. These aspects of the code can all be redesigned to improve performance.

Compared to the empirically tuned gray-zone PBL schemes (e.g., Shin and Hong 2015; Ito et al. 2015; Efstathiou et al. 2016), the proposed method is probably too expensive to be of practical use in a high-resolution NWP model in its current form. However, it is an alternative approach to gray-zone modeling that does not require any empirical tuning. It is a general method based on flow dynamics by resolving instability in the critical layers. The method could be extended to modeling the shear instability gray zone, for example, by laying a fine nest layer over the critical shear layer. In this regard, our method is better than the modified PBL schemes based on empirical flux partition functions.

6. Summary and overall assessment

This paper implements a grid-refinement-based approach for improving CBL simulations in the gray zone of PBL parameterization. The core component of the algorithm is a two-way interactive vertical nest of increased horizontal resolution near the surface. Such a fine-resolution nest serves to significantly improve the modeling of near-surface turbulent convective eddies in the CBL and associated vertical fluxes. Effectively, the strategy employs an LES-type simulation within the surface and near-surface layer while relying on PBL schemes for vertical mixing in the CBL. Special care is taken in the interpolation and antinterpolation procedures between the parent and the nested grids to ensure the conservation of mass and vertical fluxes. As a result, smoothness and continuity are obtained in the simulated

vertical flux profiles across the nesting interface. CBL parameterization aside, the algorithm is also applicable to general grid nesting practices. Future work is planned to expand the two-way interactive nesting capability in ARPS to all three dimensions.

A posteriori tests are performed to simulate an idealized CBL. Compared to the stand-alone simulations with 900-m horizontal grid spacing, the nested simulations explicitly resolve convection in the near-surface nest domain early on and produce more realistic convective structures in the entire CBL. Most notably, the onset of convection and early CBL growth (Figs. 5 and 6) are significantly improved, and the unphysical pulsing of SA900 is ameliorated. This is an important improvement, especially considering potential feedbacks with clouds and the land surface models. Between the two nest domain depths tested, the 16-level nest outperforms the 6-level nest in terms of the agreement in higher-order statistics with those of the benchmark LES. Further increasing the nesting ratio from 5:1 to 9:1 produces modest improvements, indicating a certain degree of convergence of model results for the given parent grid.

One notable deficiency of the proposed approach is the contamination of convective structures due to the coarse-resolution parent grid, especially when the nest domain is shallow. The N180-L6 run with a 5:1 nesting ratio and a six-level nest produces a spectrum that initially agrees with the high-resolution LES benchmark for wavelength resolvable by the nested grid, but the spectrum can be contaminated by the distorted convection on the 900-m parent grid. The spectrum exhibits double-peak behavior with a physical one at a shorter wavelength and a spurious longer-wavelength peak that is influenced by the coarse-resolution grid. Later in the afternoon, the spurious peak can overtake the physical peak even within the nested high-resolution domain. In this case, the simulated flow fields show convective cell structures that are similar to those in SA900 but with more details at the small scales. In comparison, using 16 levels of nesting that covers about half of the CBL depth in N180-L16, the simulation results are much improved. In this case, no spurious peak is found even at half of the CBL depth. The simulated spectra agree well with those of the LES benchmark for wavelengths that can be resolved by the grid, although there tends to be some excessive energy near the longer-wavelength end of the spectra.

Overall, the grid-refinement-based approach improves the CBL simulation in the gray zone of PBL parameterization. The method does not rely on empirically determined partition functions as used in some recently proposed grid-aware PBL schemes, and in theory, it can work with all existing PBL schemes. It is suggested that a combination of a TKE-based PBL scheme on the coarse-resolution

parent grid and a consistent TKE-based LES closure on the nested grid is preferred over first-order parameterizations because of the additional interaction of the two grids through prognostic TKE. An assessment of the added computational cost of the proposed approach is presented. Further testing of the approach in realistic simulations is required to fully demonstrate its potential.

Acknowledgments. We are grateful to Prof. Tina Chow for her help with reviewing the manuscript. We gratefully acknowledge the High Performance Computing Center (HPCC) of Nanjing University for doing the numerical calculations in this paper on its IBM Blade cluster system. Bowen Zhou is supported by the National Natural Science Foundation of China (Grant 41505047), the Dengfeng Program of Nanjing University, and a collaborative project on PBL parameterizations with the Beijing Urban Meteorology Institute. Kefeng Zhu is also supported by the Foundation of China Meteorological Administration (Grant GYHY201506006) and the National Science Foundation of China (Grant 41405100). All authors are also supported by the Research 973 Program of China (2013CB430103).

REFERENCES

- Arakawa, A., J. H. Jung, and C. M. Wu, 2011: Toward unification of the multiscale modeling of the atmosphere. *Atmos. Chem. Phys.*, **11**, 3731–3742, <https://doi.org/10.5194/acp-11-3731-2011>.
- Bougeault, P., and P. Lacarrere, 1989: Parameterization of orography-induced turbulence in a mesobeta-scale model. *Mon. Wea. Rev.*, **117**, 1872–1890, [https://doi.org/10.1175/1520-0493\(1989\)117<1872:POOITI>2.0.CO;2](https://doi.org/10.1175/1520-0493(1989)117<1872:POOITI>2.0.CO;2).
- Brasseur, J. G., and T. Wei, 2010: Designing large-eddy simulation of the turbulent boundary layer to capture law-of-the-wall scaling. *Phys. Fluids*, **22**, 021303, <https://doi.org/10.1063/1.3319073>.
- Caughey, S. J., and S. G. Palmer, 1979: Some aspects of turbulence structure through the depth of the convective boundary layer. *Quart. J. Roy. Meteor. Soc.*, **105**, 811–827, <https://doi.org/10.1002/qj.49710544606>.
- Ching, J., R. Rotunno, M. LeMone, A. Martilli, B. Kosovic, P. A. Jimenez, and J. Dudhia, 2014: Convectively induced secondary circulations in fine-grid mesoscale numerical weather prediction models. *Mon. Wea. Rev.*, **142**, 3284–3302, <https://doi.org/10.1175/MWR-D-13-00318.1>.
- Chow, F. K., R. L. Street, M. Xue, and J. H. Ferziger, 2005: Explicit filtering and reconstruction turbulence modeling for large-eddy simulation of neutral boundary layer flow. *J. Atmos. Sci.*, **62**, 2058–2077, <https://doi.org/10.1175/JAS3456.1>.
- Clark, T., and R. Farley, 1984: Severe downslope windstorm calculations in 2 and 3 spatial dimensions using anelastic interactive grid nesting: A possible mechanism for gustiness. *J. Atmos. Sci.*, **41**, 329–350, [https://doi.org/10.1175/1520-0469\(1984\)041<0329:SDWCIT>2.0.CO;2](https://doi.org/10.1175/1520-0469(1984)041<0329:SDWCIT>2.0.CO;2).
- Clarke, R. H., A. J. Dyer, R. R. Brook, D. G. Reid, and A. J. Troup, 1971: The Wangara experiment: Boundary layer data. CSIRO Division of Meteorological Physics Tech. Paper 19, 340 pp.

- Daniels, M. H., K. A. Lundquist, J. D. Mirocha, D. J. Wiersema, and F. K. Chow, 2016: A new vertical grid nesting capability in the Weather Research and Forecasting (WRF) Model. *Mon. Wea. Rev.*, **144**, 3725–3747, <https://doi.org/10.1175/MWR-D-16-0049.1>.
- Deardorff, J., 1974: Three-dimensional numerical study of the height and mean structure of a heated planetary boundary layer. *Bound.-Layer Meteor.*, **7**, 81–106, <https://doi.org/10.1007/BF00224974>.
- Efstathiou, G. A., R. J. Beare, S. Osborne, and A. P. Lock, 2016: Grey zone simulations of the morning convective boundary layer development. *J. Geophys. Res. Atmos.*, **121**, 4769–4782, <https://doi.org/10.1002/2016JD024860>.
- Gentine, P., G. Bellon, and C. C. van Heerwaarden, 2015: A closer look at boundary layer inversion in large-eddy simulations and bulk models: Buoyancy-driven case. *J. Atmos. Sci.*, **72**, 728–749, <https://doi.org/10.1175/JAS-D-13-0377.1>.
- Gibbs, J. A., E. Fedorovich, and A. M. J. van Eijk, 2011: Evaluating Weather Research and Forecasting (WRF) Model predictions of turbulent flow parameters in a dry convective boundary layer. *J. Appl. Meteor. Climatol.*, **50**, 2429–2444, <https://doi.org/10.1175/2011JAMC2661.1>.
- Harris, L. M., and D. R. Durran, 2010: An idealized comparison of one-way and two-way grid nesting. *Mon. Wea. Rev.*, **138**, 2174–2187, <https://doi.org/10.1175/2010MWR3080.1>.
- Holtstlag, A. M., and C.-H. Moeng, 1991: Eddy diffusivity and countergradient transport in the convective atmospheric boundary layer. *J. Atmos. Sci.*, **48**, 1690–1698, [https://doi.org/10.1175/1520-0469\(1991\)048<1690:EDACTI>2.0.CO;2](https://doi.org/10.1175/1520-0469(1991)048<1690:EDACTI>2.0.CO;2).
- Hong, S.-Y., Y. Noh, and J. Dudhia, 2006: A new vertical diffusion package with an explicit treatment of entrainment processes. *Mon. Wea. Rev.*, **134**, 2318–2341, <https://doi.org/10.1175/MWR3199.1>.
- Honnert, R., V. Masson, and F. Couvreux, 2011: A diagnostic for evaluating the representation of turbulence in atmospheric models at the kilometer scale. *J. Atmos. Sci.*, **68**, 3112–3131, <https://doi.org/10.1175/JAS-D-11-061.1>.
- Hunt, J. C. R., J. C. Kaimal, and J. E. Gaynor, 1988: Eddy structure in the convective boundary layer—New measurements and new concepts. *Quart. J. Roy. Meteor. Soc.*, **114**, 827–858, <https://doi.org/10.1002/qj.49711448202>.
- Huq, S., F. De Roo, S. Raasch, and M. Mauder, 2014: Vertical grid nesting for improved surface layer resolution in large-eddy simulation. *21st Symp. on Boundary Layers and Turbulence*, Leeds, United Kingdom, Amer. Meteor. Soc., 9B.6, <https://ams.confex.com/ams/21BLT/webprogram/Paper247755.html>.
- Ito, J., H. Niino, M. Nakanishi, and C.-H. Moeng, 2015: An extension of the Mellor–Yamada model to the terra incognita zone for dry convective mixed layers in the free convection regime. *Bound.-Layer Meteor.*, **157**, 23–43, <https://doi.org/10.1007/s10546-015-0045-5>.
- Kaimal, J. C., and J. J. Finnigan, 1994: *Atmospheric Boundary Layer Flows: Their Structure and Measurement*. Oxford University Press, 289 pp.
- Klemp, J. B., and R. B. Wilhelmson, 1978: The simulation of three-dimensional convective storm dynamics. *J. Atmos. Sci.*, **35**, 1070–1096, [https://doi.org/10.1175/1520-0469\(1978\)035<1070:TSOTDC>2.0.CO;2](https://doi.org/10.1175/1520-0469(1978)035<1070:TSOTDC>2.0.CO;2).
- Kurihara, Y., G. Tripoli, and M. Bender, 1979: Design of a movable nested-mesh primitive equation model. *Mon. Wea. Rev.*, **107**, 239–249, [https://doi.org/10.1175/1520-0493\(1979\)107<0239:DOANM>2.0.CO;2](https://doi.org/10.1175/1520-0493(1979)107<0239:DOANM>2.0.CO;2).
- Lenschow, D. H., and B. B. Stankov, 1986: Length scales in the convective boundary layer. *J. Atmos. Sci.*, **43**, 1198–1209, [https://doi.org/10.1175/1520-0469\(1986\)043<1198:LSITCB>2.0.CO;2](https://doi.org/10.1175/1520-0469(1986)043<1198:LSITCB>2.0.CO;2).
- Lilly, D., 1967: The representation of small-scale turbulence in numerical simulation experiments. *Proc. IBM Scientific Symp. on Environmental Science*, White Plains, NY, IBM, 195–210.
- Lundquist, K. A., M. H. Daniels, J. D. Mirocha, D. J. Wiersema, and F. K. Chow, 2016: A new vertical grid nesting capability for multiscale simulations using the WRF Model. *22nd Symp. on Boundary Layers and Turbulence*, Salt Lake City, UT, Amer. Meteor. Soc., 3B.5, <https://ams.confex.com/ams/32AgF22BLT3BG/webprogram/Paper295892.html>.
- Mahrt, L., 2014: Stably stratified atmospheric boundary layers. *Annu. Rev. Fluid Mech.*, **46**, 23–45, <https://doi.org/10.1146/annurev-fluid-010313-141354>.
- Mirocha, J., G. Kirkil, E. Bou-Zeid, F. K. Chow, and B. Kosovic, 2013: Transition and equilibration of neutral atmospheric boundary layer flow in one-way nested large-eddy simulations using the Weather Research and Forecasting Model. *Mon. Wea. Rev.*, **141**, 918–940, <https://doi.org/10.1175/MWR-D-11-00263.1>.
- Moeng, C. H., J. Dudhia, J. B. Klemp, and P. P. Sullivan, 2007: Examining two-way grid nesting for large eddy simulation of the PBL using the WRF Model. *Mon. Wea. Rev.*, **135**, 2295–2311, <https://doi.org/10.1175/MWR3406.1>.
- Muñoz-Esparza, D., B. Kosović, J. Mirocha, and J. van Beeck, 2014: Bridging the transition from mesoscale to microscale turbulence in numerical weather prediction models. *Bound.-Layer Meteor.*, **153**, 409–440, <https://doi.org/10.1007/s10546-014-9956-9>.
- , J. K. Lundquist, J. A. Sauer, B. Kosović, and R. R. Linn, 2017: Coupled mesoscale-LES modeling of a diurnal cycle during the CWEX-13 field campaign: From weather to boundary-layer eddies. *J. Adv. Model. Earth Syst.*, **9**, 1572–1594, <https://doi.org/10.1002/2017MS000960>.
- Pielke, R. A., and Coauthors, 1992: A comprehensive meteorological modeling system—RAMS. *Meteor. Atmos. Phys.*, **49**, 69–91, <https://doi.org/10.1007/BF01025401>.
- Shin, H. H., and S.-Y. Hong, 2013: Analysis of resolved and parameterized vertical transports in convective boundary layers at gray-zone resolutions. *J. Atmos. Sci.*, **70**, 3248–3261, <https://doi.org/10.1175/JAS-D-12-0290.1>.
- , and —, 2015: Representation of the subgrid-scale turbulent transport in convective boundary layers at gray-zone resolutions. *Mon. Wea. Rev.*, **143**, 250–271, <https://doi.org/10.1175/MWR-D-14-00116.1>.
- , and J. Dudhia, 2016: Evaluation of PBL parameterizations in WRF at subkilometer grid spacings: Turbulence statistics in the dry convective boundary layer. *Mon. Wea. Rev.*, **144**, 1161–1177, <https://doi.org/10.1175/MWR-D-15-0208.1>.
- Skamarock, W. C., and Coauthors, 2008: A description of the Advanced Research WRF version 3. NCAR Tech. Note NCAR/TN-475+STR, 113 pp., <https://doi.org/10.5065/D68S4MVH>.
- Stull, R. B., 1988: *An Introduction to Boundary Layer Meteorology*. Kluwer Academic Publishers, 666 pp.
- Sullivan, P. P., J. C. McWilliams, and C. H. Moeng, 1996: A grid nesting method for large-eddy simulation of planetary boundary-layer flows. *Bound.-Layer Meteor.*, **80**, 167–202, <https://doi.org/10.1007/BF00119016>.
- Sun, W. Y., and C. Z. Chang, 1986: Diffusion model for a convective layer. 1. Numerical simulation of convective boundary layer. *J. Climate Appl. Meteor.*, **25**, 1445–1453, [https://doi.org/10.1175/1520-0450\(1986\)025<1445:DMFACL>2.0.CO;2](https://doi.org/10.1175/1520-0450(1986)025<1445:DMFACL>2.0.CO;2).
- Troen, I., and L. Mahrt, 1986: A simple model of the atmospheric boundary-layer; sensitivity to surface evaporation. *Bound.-Layer Meteor.*, **37**, 129–148, <https://doi.org/10.1007/BF00122760>.
- Walko, R. L., C. J. Trempack, R. A. Pielke, and W. R. Cotton, 1995: An interactive nesting algorithm for stretched grids and variable

- nesting ratios. *J. Appl. Meteor.*, **34**, 994–999, [https://doi.org/10.1175/1520-0450\(1995\)034<0994:AINAFS>2.0.CO;2](https://doi.org/10.1175/1520-0450(1995)034<0994:AINAFS>2.0.CO;2).
- Wyngaard, J. C., 2004: Toward numerical modeling in the “terra incognita.” *J. Atmos. Sci.*, **61**, 1816–1826, [https://doi.org/10.1175/1520-0469\(2004\)061<1816:TNMITT>2.0.CO;2](https://doi.org/10.1175/1520-0469(2004)061<1816:TNMITT>2.0.CO;2).
- Xue, M., K. K. Droegemeier, V. Wong, A. Shapiro, and K. Brewster, 1995: Advanced regional prediction system ARPS version 4.0 user’s guide. Center for Analysis and Prediction of Storms Tech. Rep., 398 pp.
- , J. Zong, and K. K. Droegemeier, 1996: Parameterization of PBL turbulence in a multi-scale nonhydrostatic model. Preprints, *11th Conf. on Numerical Weather Prediction*, Norfolk, VA, Amer. Meteor. Soc., 363–365.
- , K. K. Droegemeier, and V. Wong, 2000: The Advanced Regional Prediction System (ARPS)—A multi-scale nonhydrostatic atmospheric simulation and prediction model. Part I: Model dynamics and verification. *Meteor. Atmos. Phys.*, **75**, 161–193, <https://doi.org/10.1007/s007030070003>.
- , and Coauthors, 2001: The Advanced Regional Prediction System (ARPS)—A multi-scale nonhydrostatic atmospheric simulation and prediction tool. Part II: Model physics and applications. *Meteor. Atmos. Phys.*, **76**, 143–165, <https://doi.org/10.1007/s007030170027>.
- Yamada, T., and G. Mellor, 1975: Simulation of Wangara atmospheric boundary layer data. *J. Atmos. Sci.*, **32**, 2309–2329, [https://doi.org/10.1175/1520-0469\(1975\)032<2309:ASOTWA>2.0.CO;2](https://doi.org/10.1175/1520-0469(1975)032<2309:ASOTWA>2.0.CO;2).
- Zhong, S., and F. Chow, 2012: Meso- and fine-scale modeling over complex terrain: Parameterizations and applications. *Mountain Weather Research and Forecasting: Recent Progress and Current Challenges*, F. Chow, S. F. De Wekker, and B. Synder, Eds., Springer, 591–654.
- Zhou, B., and F. K. Chow, 2013: Nighttime turbulent events in a steep valley: A nested large-eddy simulation study. *J. Atmos. Sci.*, **70**, 3262–3276, <https://doi.org/10.1175/JAS-D-13-02.1>.
- , J. S. Simon, and F. K. Chow, 2014: The convective boundary layer in the terra incognita. *J. Atmos. Sci.*, **71**, 2545–2563, <https://doi.org/10.1175/JAS-D-13-0356.1>.
- , M. Xue, and K. Zhu, 2017: A grid-refinement-based approach for modeling the convective boundary layer in the gray zone: A pilot study. *J. Atmos. Sci.*, **74**, 3497–3513, <https://doi.org/10.1175/JAS-D-16-0376.1>.